nature electronics

ARTICLES

https://doi.org/10.1038/s41928-020-00493-6

Check for updates

An epicardial bioelectronic patch made from soft rubbery materials and capable of spatiotemporal mapping of electrophysiological activity

Kyoseung Sim[1,2,10], Faheem Ershad[3,10], Yongcao Zhang[4,10], Pinyi Yang[1], Hyunseok Shim[4], Zhoulyu Rao[4], Yuntao Lu[4], Anish Thukral[1], Abdelmotagaly Elgalad[5], Yutao Xi[6], Bozhi Tian[7], Doris A. Taylor[6] and Cunjiang Yu[1,3,4,8,9] ✉

An epicardial bioelectronic patch is an important device for investigating and treating heart diseases. The ideal device should possess cardiac-tissue-like mechanical softness and deformability, and be able to perform spatiotemporal mapping of cardiac conduction characteristics and other physical parameters. However, existing patches constructed from rigid materials with structurally engineered mechanical stretchability still have a hard–soft interface with the epicardium, which can strain cardiac tissue and does not allow for deformation with a beating heart. Alternatively, patches made from intrinsically soft materials lack spatiotemporal mapping or sensing capabilities. Here, we report an epicardial bioelectronic patch that is made from materials matching the mechanical softness of heart tissue and can perform spatiotemporal mapping of electrophysiological activity, as well as strain and temperature sensing. Its capabilities are illustrated on a beating porcine heart. We also show that the patch can provide therapeutic capabilities (electrical pacing and thermal ablation), and that a rubbery mechanoelectrical transducer can harvest energy from heart beats, potentially providing a power source for epicardial devices.

Implantable epicardial devices are important for discovering, monitoring, mitigating and treating cardiovascular diseases[1–4]. A typical epicardial bioelectronic device contacts with the epicardium and measures electrophysiological and physical characteristics of the heart such as electrocardiograms (ECGs), mechanical contraction and expansion behaviours, and pathophysiological information. The devices can also provide therapeutic solutions[5–7]. The ideal bioelectronic device should possess cardiac-tissue-like mechanical softness and deformability, and various sensing functions. Specifically, the device should use soft materials with properties similar to those of heart tissues to seamlessly interface with the epicardium and concurrently deform with a beating heart. It should also offer spatiotemporal mapping of the cardiac conduction characteristics[6,8–10] and other physical parameters.

Advances in materials, mechanical structure designs and bioelectronic technologies have led to the development of deformable epicardial bioelectronics. Structural engineering of rigid materials to yield mechanical softness has been an important strategy in the creation of soft epicardial devices. For instance, thin-film flexible electronics based on ultrathin silicon on a polymer film have been used to spatially map electrophysiological activities[11–13], and rigid materials have been implemented in epicardial patches with open-mesh structural designs that give overall mechanical stretchability and deformability, allowing them to deform with the heart[14,15]. However, these devices are difficult to interface with cardiomyocytes: flexible silicon electronics for cardiac mapping does not allow concurrent deformation with a beating heart[16] and mesh-structured cardiac devices based on intrinsically rigid materials can overstrain cardiomyocytes[17,18]. Similarly, soft bioelectronics approaches typically use rigid, non-stretchy materials that form a hard–soft interface with biological tissues[12,19]. An alternative route is to use intrinsically soft materials. Soft conductive composites of silver nanowires (AgNWs)/styrene–butadiene–styrene have been developed into a cardiac wrap for preserving diastolic relaxation, mechanically supporting the heart and improving cardiac contractility through electrical stimulation[20]. However, a cardiac wrap that is based solely on a continuous conductive material cannot provide spatiotemporal mapping capabilities.

In this Article, we report an epicardial bioelectronic patch that is made entirely of soft rubbery materials with moduli that are close to that of heart tissue[21–23] (tens of kPa to ~1 MPa). The patch can monitor electrophysiological activity, strain and temperature, while deforming with a beating heart. The device contains a fully rubbery transistor array that is capable of mapping biopotentials in a spatial and temporal manner by using active matrix multiplexing. The transistors are stable for a few weeks in biofluid due to encapsulation and the use of composite materials. The active matrix and a rubbery thermal actuator provide electrical pacing and thermal ablation capabilities, respectively, and a rubbery mechanoelectrical transducer allows for conversion of heart beats to electrical energy that could be potentially stored and utilized. An in vivo validation on a living porcine heart illustrates the key aspects and functionalities of the multifunctional rubbery epicardial bioelectronic patch.

[1]Department of Mechanical Engineering, University of Houston, Houston, TX, USA. [2]Department of Chemistry, Ulsan National Institute of Science and Technology (UNIST), Ulsan, Republic of Korea. [3]Department of Biomedical Engineering, University of Houston, Houston, TX, USA. [4]Materials Science and Engineering Program, University of Houston, Houston, TX, USA. [5]Center for Preclinical Surgical & Interventional Research, Texas Heart Institute, Houston, TX, USA. [6]Regenerative Medicine Research Lab, Texas Heart Institute, Houston, TX, USA. [7]Department of Chemistry, The University of Chicago, Chicago, IL, USA. [8]Department of Electrical and Computer Engineering, University of Houston, Houston, TX, USA. [9]Texas Center for Superconductivity, University of Houston, Houston, TX, USA. [10]These authors contributed equally: Kyoseung Sim, Faheem Ershad, Yongcao Zhang. ✉e-mail: cyu15@uh.edu

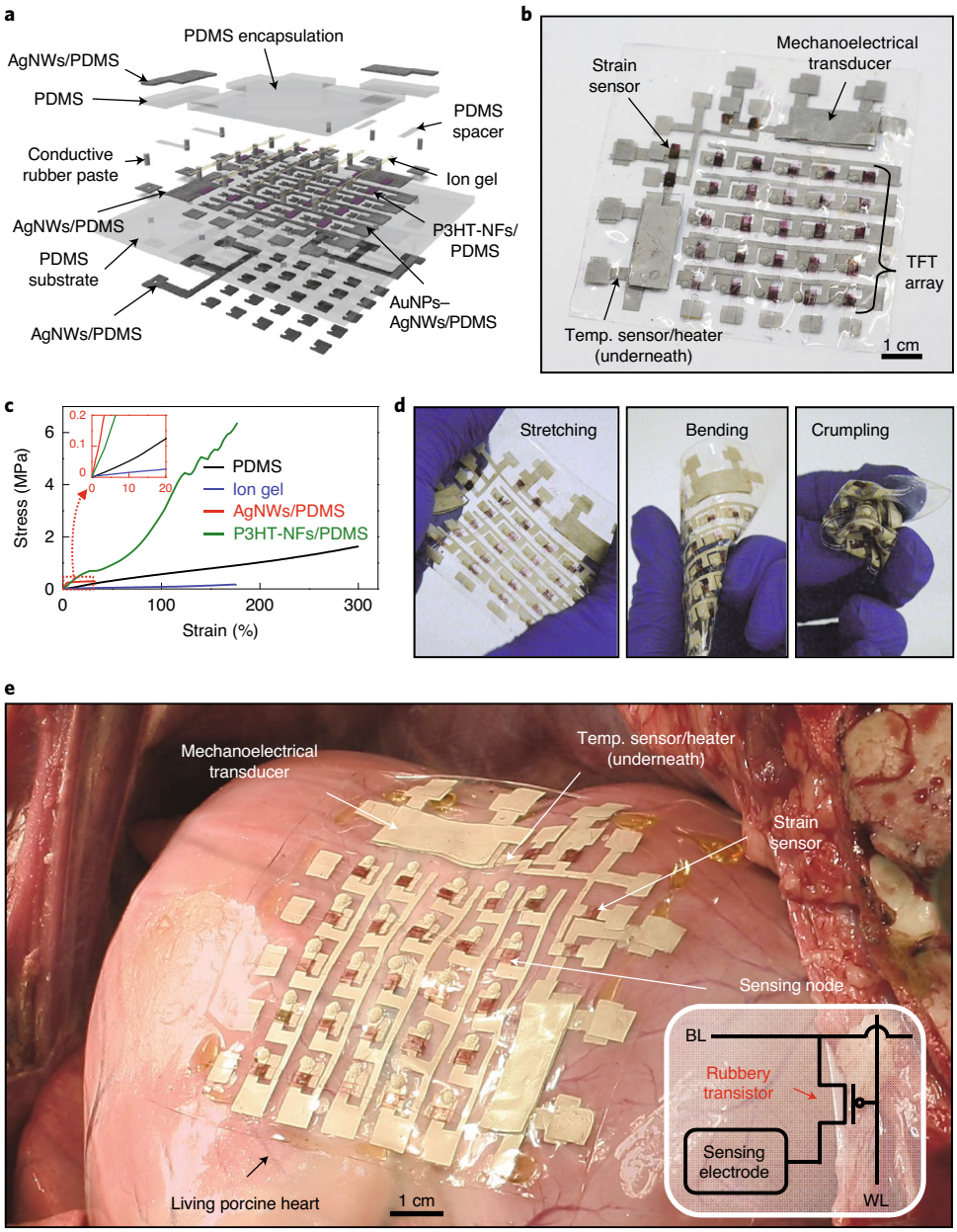

Fig. 1 | Soft rubbery epicardial bioelectronic patch. a, An exploded schematic view of the soft and stretchy epicardial bioelectronic patch. **b**, An optical image of the fabricated soft and stretchy epicardial bioelectronic patch. TFT, thin-film transistor. **c**, Strain–stress curves of the rubbery electrical components for the devices. **d**, The rubbery patch under different mechanical deformations. **e**, The rubbery patch on the epicardial surface of a living porcine heart. Inset: the circuit diagram for a single sensing node in the 5×5 active matrix. BL, bit line; WL, word line.

Multifunctional rubbery epicardial bioelectronics

The epicardial bioelectronics was constructed into a thin elastic electronic sheet with submillimetre (~400-μm) thickness, based on rubbery conductors, semiconductors and dielectrics developed through low-cost facile fabrication processes such as coating and printing. Figure 1a presents an exploded view of the soft, stretchy epicardial bioelectronic patch, which is fully made out of intrinsically soft and stretchable materials, including polydimethylsiloxane (PDMS) as the substrate/encapsulation, conductive rubbery paste as interconnections, AgNWs embedded in PDMS (AgNWs/PDMS) as the rubbery conductor, poly(3-hexylthiophene-2,5-diyl) nanofibrils (P3HT-NFs)/PDMS as the rubbery semiconductor, and ion gel as the rubbery dielectric[24–26]. The fabricated epicardial bioelectronics containing a rubbery transistor array, strain sensor, temperature sensor/thermal actuator and mechanoelectrical transducer for epicardial sensing, stimulating and energy harvesting is shown in Fig. 1b. The bioelectronics was fabricated from double-sided embedding of AgNWs in thin PDMS (thickness of ~350 μm). The double-sided embedding involved adhering two different electrode patterns for the top and bottom electrodes before curing the PDMS for one of the electrode patterns. The preparation of the double-sided electrodes is detailed in Methods and Supplementary Fig. 1. To build the transistors and strain sensors, gold nanoparticles (AuNPs) were conformally coated on AgNWs/PDMS through a galvanic replacement process to minimize the energy barrier between the P3HT-based rubbery semiconductor and AgNW/PDMS electrode to form an ohmic contact[26,27]. Thereafter the P3HT-NFs/PDMS, via holes, conductive rubber paste, ion gel and PDMS encapsulation layers, were formed sequentially, followed by placement of the final layers of AgNWs/PDMS for the top electrode of the rubbery

mechanoelectrical transducer. Methods and Supplementary Fig. 2 describe and schematically illustrate the detailed fabrication process of the epicardial bioelectronic patch, respectively.

As emphasized earlier, the material stiffness should be similar to that of the native epicardium to allow for improved interfacing. The strain–stress curves of all materials used to construct the rubbery devices show excellent rubber-like mechanical softness, with low Young's moduli of 6.60 MPa, 2.78 MPa and 133 kPa for the AgNWs/PDMS conductor, P3HT-NFs/PDMS semiconductor and ion-gel gate dielectric, respectively. All of the moduli are comparable to that of the commonly utilized elastomer PDMS as the substrate (15:1 weight ratio of base and curing agent, Young's modulus 0.70 MPa) and porcine heart tissue, as shown in Fig. 1c and Supplementary Fig. 3, respectively. It is also noted that the moduli of the right and left ventricles of the heart tissues are similar[28]. Figure 1d shows various mechanical deformations of the epicardial bioelectronic patch, including stretching, bending and crumpling. The rubbery devices showed no physical damage in response to the deformations due to the rubber-like nature of all the materials used for device construction. Owing to their mechanical softness, the devices can be conformally placed on the epicardial surface of a living porcine heart as demonstrated in Fig. 1e. The rubbery active-matrix multiplexed epicardial patch has 25 sensing nodes arranged in the format of a 5 × 5 array for ECG mapping. An individual sensing node is shown in the inset of Fig. 1e. The nodes are connected to the bottom electrode by conductive rubber paste, which is shown in Supplementary Fig. 4.

Characterization of the rubbery devices

The rubbery transistor is the key component to construct an active matrix array, enabling multiplexed spatial and temporal mapping of electrophysiological signals. The rubbery transistor was constructed based on the AuNP-coated AgNWs/PDMS electrode (AuNPs–AgNWs/PDMS), P3HT-NFs/PDMS and ion gel as the conductor, semiconductor and gate dielectric, respectively, as shown in Fig. 2a. The fabrication process of the transistor is described in Supplementary Information. Figure 2b shows the output curves featuring typical p-channel characteristics. It is noted that the transistor shows slight hysteresis (Supplementary Fig. 5), which is similar to those shown in recently reported ion-gated transistors[29,30]. Further optimizations such as reducing the thickness of the semiconductor and the scan rate can be implemented to minimize hysteresis[31]. The rubbery transistor can be stretched by 30% and still function, as shown in Fig. 2c. It is noted that upon stretching, slight changes in field-effect mobility (μ_{FE}), threshold voltage (V_{TH}) and on/off ratio (I_{on}/I_{off}) from 1.245 $cm^2 V^{-1} s^{-1}$ to 0.579 $cm^2 V^{-1} s^{-1}$, −1.735 V to −1.678 V and 5.247×10^3 to 9.243×10^2 respectively, and a moderate recovery of the values after releasing back to a strain of 0%, are observed (Fig. 2c and Supplementary Fig. 6). The degradation is mainly due to the rupture of the P3HT-NFs upon stretching[26]. It is noted that fully stretchable transistors and electronics based on other electronic materials and device structures as reported elsewhere[24,32–35] could potentially be devised for a soft epicardial patch with spatiotemporal mapping capabilities.

Alongside monitoring the electrical activity of the heart, measuring the strain of the epicardium is another critical approach to examine cardiac health. Cardiac disorders (that is, myocardial ischaemia) could be diagnosed through tracking the changes in mechanical strain[36,37]. The rubbery strain sensors can provide important information about the systolic and diastolic strains of the heart[38,39]. Figure 2d shows a schematic exploded view (left) and optical image (right) of the rubbery strain sensor employing AuNPs–AgNWs/PDMS and P3HT-NFs/PDMS as the conductor and sensing material, respectively. The fabrication process is described in Supplementary Information. The normalized resistance change depending on strain from 0% to 30% (Fig. 2e) reveals high stretchability and a high gauge factor of 7.76 compared with the recently reported strain gauges used in cardiac health studies[13,14]. The response time of the strain sensor is 0.2 s. Figure 2f shows the stable normalized resistance change under repeated stretching and releasing at 30% strain. It is noted that the sensing property of the rubbery strain sensor saturated after five cycles of stretching and releasing and is stable for more than 300 cycles, as shown in Supplementary Fig. 7.

Besides strain, temperature is another important cardiac parameter and can be used to reveal arrhythmias[40]. Epicardial temperature monitoring is an important technique for cardiac healthcare and can be achieved by the rubbery temperature sensor. The resistive temperature sensor was fabricated in the same manner as the rubbery conductor. A schematic illustration and optical image are shown in Fig. 2g. The narrower portion of the electrode pattern had a higher resistance than that of the other electrode parts, which allowed for a defined sensing area. The temperature sensing property was characterized by measuring the resistance at different temperatures. Figure 2h shows the normalized resistance change at different temperatures in the range of 27 °C to 45 °C under mechanical strains of 0% and 30%, which proves that there was no substantial impact on the sensing properties from the mechanical deformation. The sensitivities of the rubbery temperature sensor were 0.35% $°C^{-1}$ and 0.38% $°C^{-1}$ under strains of 0% and 30%, respectively, which are comparable to those of metal thin-film-based temperature sensors used for epicardial temperature monitoring[13,14]. The response time of the temperature sensor is 1.53 s. The resistance change of the rubbery temperature sensor depending on temperature is shown in Supplementary Fig. 8.

Localized heating was also investigated, as thermal ablation is a common treatment to destroy tissue that impedes the conduction system of the heart[41,42]. The rubbery thermal actuator was developed to serve this purpose. The resistive thermal actuator, designed in the same pattern as the temperature sensor, was characterized by measuring the temperature change upon applying d.c. bias (ranging from 1 to 3.5 V) as shown in Fig. 2i and Supplementary Fig. 9. Typical Joule heating characteristics of around 68 °C at 3.5 V can be produced, which is sufficient for thermal ablation[43,44]. Due to the inversely proportional relationship between Joule heating and resistance, the temperatures at certain applied voltages show a slight change because of the minor resistance change under mechanical strain (Supplementary Fig. 8).

Mechanoelectrical transducers that harvest heart beating could serve as possible and sustainable power sources for epicardial devices[45]. All rubbery materials were used to construct the mechanoelectrical transducer, which operated on the basis of the triboelectric effect in vertical contact-separation mode, shown in a schematic exploded view (left) and an optical image (right) in Fig. 2j. The device fabrication involved the assembly of two thin AgNWs/PDMS electrodes with thin spacers placed in between the electrode layers: further details of the fabrication are described in Supplementary Information. The rubbery mechanoelectrical transducer in vertical contact-separation mode generates electricity through the relative motion change of the two vertically placed triboelectric layers. Under mechanical deformation, unique coupling between triboelectrification and electrostatic induction generates electron flow between the two electrodes, leading to electricity generation[46,47]. Upon undergoing a mechanical strain of 30%, the open-circuit voltage (V_{oc}) and short-circuit current (I_{sc}) of the harvester reached ~1.47 V and ~86 nA, respectively, under a load resistance of 92 MΩ (Fig. 2k,l). The V_{oc}, I_{sc} and output power at different load resistances are shown in Supplementary Figs. 10 and 11.

Rubbery active matrix for ECG sensor array

The rubbery transistor serves as a switching element in the active matrix for multiplexing. The ECG sensing capability from

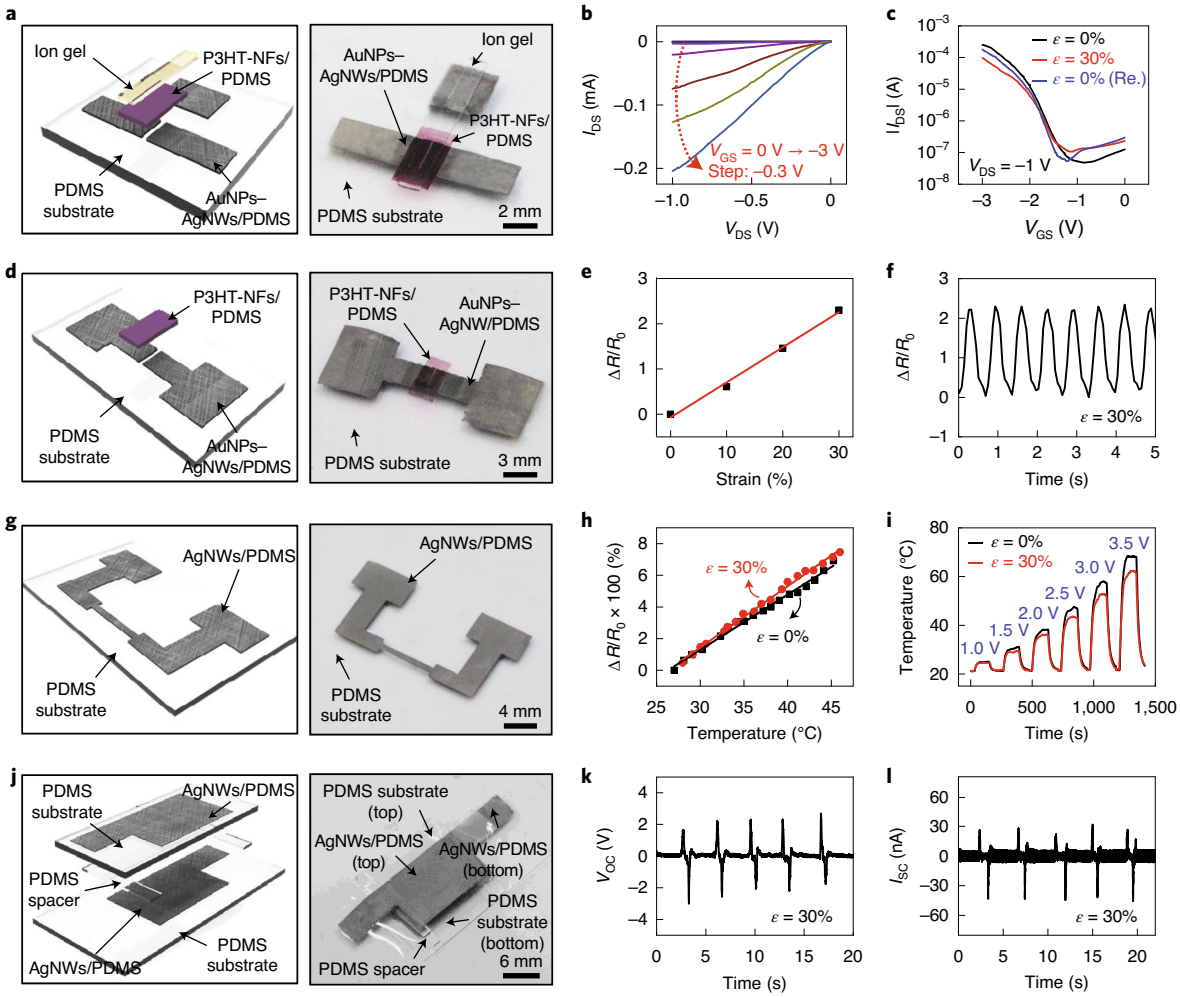

Fig. 2 | Characteristics of the individual devices on the epicardial bioelectronic patch. a, Schematic exploded view (left) and optical image (right) of the rubbery transistor. **b**, Output characteristics of the rubbery transistor. I_{DS}, drain–source current; V_{DS}, drain–source voltage; V_{GS}, gate–source voltage. **c**, Transfer characteristics of the rubbery transistor with and without mechanical strain. Re., released. **d**, Schematic exploded view (left) and optical image (right) of the rubbery strain sensor. **e**, Calibration curve of the rubbery strain sensor. **f**, Dynamic relative resistance change ($\Delta R/R_0$) of the rubbery strain sensor under cyclic stretching and relaxing. **g**, Schematic illustration (left) and optical image (right) of the rubbery temperature sensor/rubbery heater. **h**, Characterization plot of the temperature sensor with and without mechanical strain. **i**, Dynamic temperature change of the rubbery heater under different applied voltages with and without mechanical strain. **j**, Schematic exploded view (left) and optical image (right) of the rubbery mechanoelectrical transducer. **k**,**l**, Open-circuit voltage (**k**) and short-circuit current (**l**) of the rubbery mechanoelectrical transducer.

the individual channels of the rubbery active matrix was carefully characterized (Fig. 3a). The operating property of the sensing node was evaluated by calculating the voltage gain from the ratio of the output and input voltages (V_{OUT}/V_{IN}). Figure 3b presents the sinusoidal input and output voltages with a voltage gain of 0.968 at an amplitude and frequency of 10 mV and 1 Hz, respectively. No signal distortion of the output voltage was observed. The input voltage, output voltage and gain depending on frequency at a constant amplitude of 10 mV are plotted in Fig. 3c. The sinusoidal input and output curves at different frequencies are shown in Supplementary Fig. 12. It is noted that frequencies up to 2 Hz were tested because they are relevant to the heartbeat rate. The consistency of the gain demonstrates the stable operation of the rubbery transistor at different frequencies. Similarly, no notable gain variation was observed in the amplitude range from 2 mV to 1 V at a constant frequency of 1 Hz, as shown in Fig. 3d and Supplementary Fig. 13. Considering that the ideal value of the gain is 1, the gains we obtained here (>0.9) indicate that our rubbery active matrix can adequately perform epicardial ECG sensing[11].

In addition to characterizing the rubbery transistor under mechanical stretching as described above, the sensing properties were also investigated under bending because of the three-dimensional curvilinear shape of the heart. Figure 3e shows the representative images of the device in flat (top left), stretched (bottom left) and bent (right) states. The device characteristics at different bending radii are shown in Supplementary Fig. 14; there were no notable changes under bending radii up to 1.3 cm. The gain was maintained, and no substantial voltage loss was observed, under mechanical deformations including bending ($r = 1.3$ cm) and stretching (mechanical strain $\varepsilon = 30\%$), as shown in Fig. 3f and Supplementary Fig. 15. The single-channel sensing was further validated by extracting the ECG when the device was worn on the chest (Supplementary Fig. 16).

Aside from the mechanical considerations, biofluids are another factor that could potentially affect device performance[11]. Thus, long-term stability in biofluid was evaluated to ensure successful operation of the rubbery transistor in vivo. PDMS was chosen as the encapsulation material due to its mechanical softness, easy

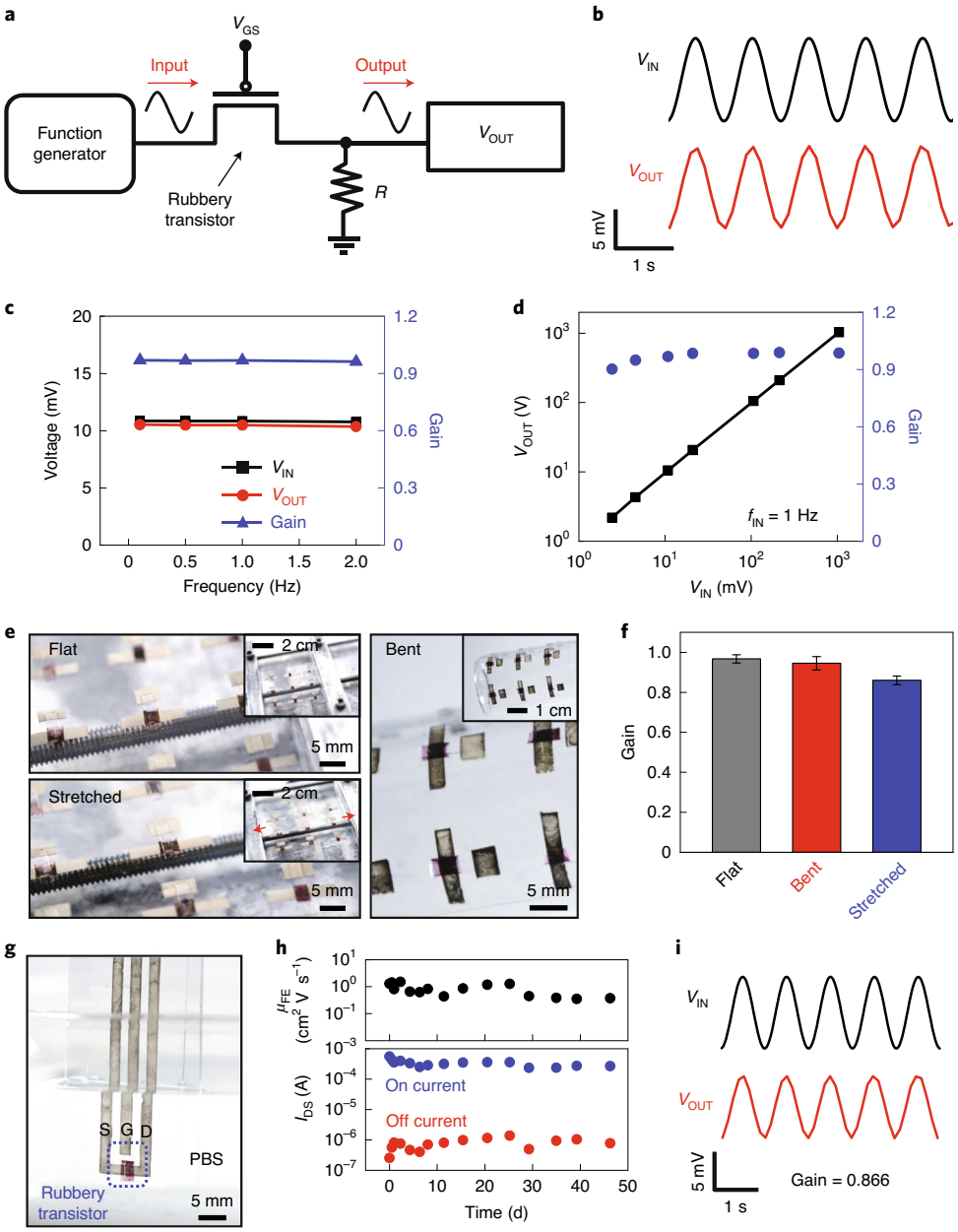

Fig. 3 | Validation of the sensing system based on the rubbery transistor. a, Circuit diagram for validation of the sensing system (R = 100 kΩ). **b**, Sinusoidal input and output signal through the sensing system. **c**, Input voltage, output voltage and ratio under different input frequencies. **d**, Output voltage and ratio under different amplitudes of input voltage at a frequency (f_{IN}) of 1 Hz. **e**, Optical images of the rubbery transistor under mechanical deformations of stretching and bending. The insets are zoomed-out images of each deformation. **f**, The input and output voltage ratio under mechanical deformation of stretching and bending (n = 20). Data are presented as mean ± s.d. **g**, Optical image of the rubbery transistor in PBS. S, source; G, gate; D, drain. **h**, The field effect mobility and on and off currents during the soaking test for 46 d. **i**, Sinusoidal input and output signal through the sensing system after the 46-d soaking test.

applicability and hydrophobicity as a moisture barrier. The rubbery transistor with a ~100-μm-thick PDMS encapsulation layer was characterized by completely immersing the device into a phosphate-buffered saline (PBS) solution maintained at a physiologically relevant temperature (37 °C). Figure 3g shows an optical image of the rubbery transistor in the PBS solution for the soaking test. As shown in Fig. 3h, the device continued to operate normally with no substantial degradation of properties such as μ_{FE}, I_{on} or I_{off} for 46 d. The transfer curves, V_{TH} and I_{on}/I_{off} of the device during the soaking test are plotted in Supplementary Fig. 17. Figure 3i shows the response of a sensing node based on the rubbery transistor in PBS after 46 d, which maintained a high gain of 0.866. All these results clearly prove the applicability and reliability of the rubbery transistor-based ECG sensing node for sustainable in vivo cardiac implantation operation.

In vivo epicardial electrophysiological mapping

Since many critical heart diseases such as cardiac arrhythmias can occur over all ranges of the three-dimensional cardiac surface, epicardial electrophysiological mapping is very important to the diagnosis and treatment of heart conditions[48]. Specifically, spatial and temporal mapping over large areas of the heart can reveal portions

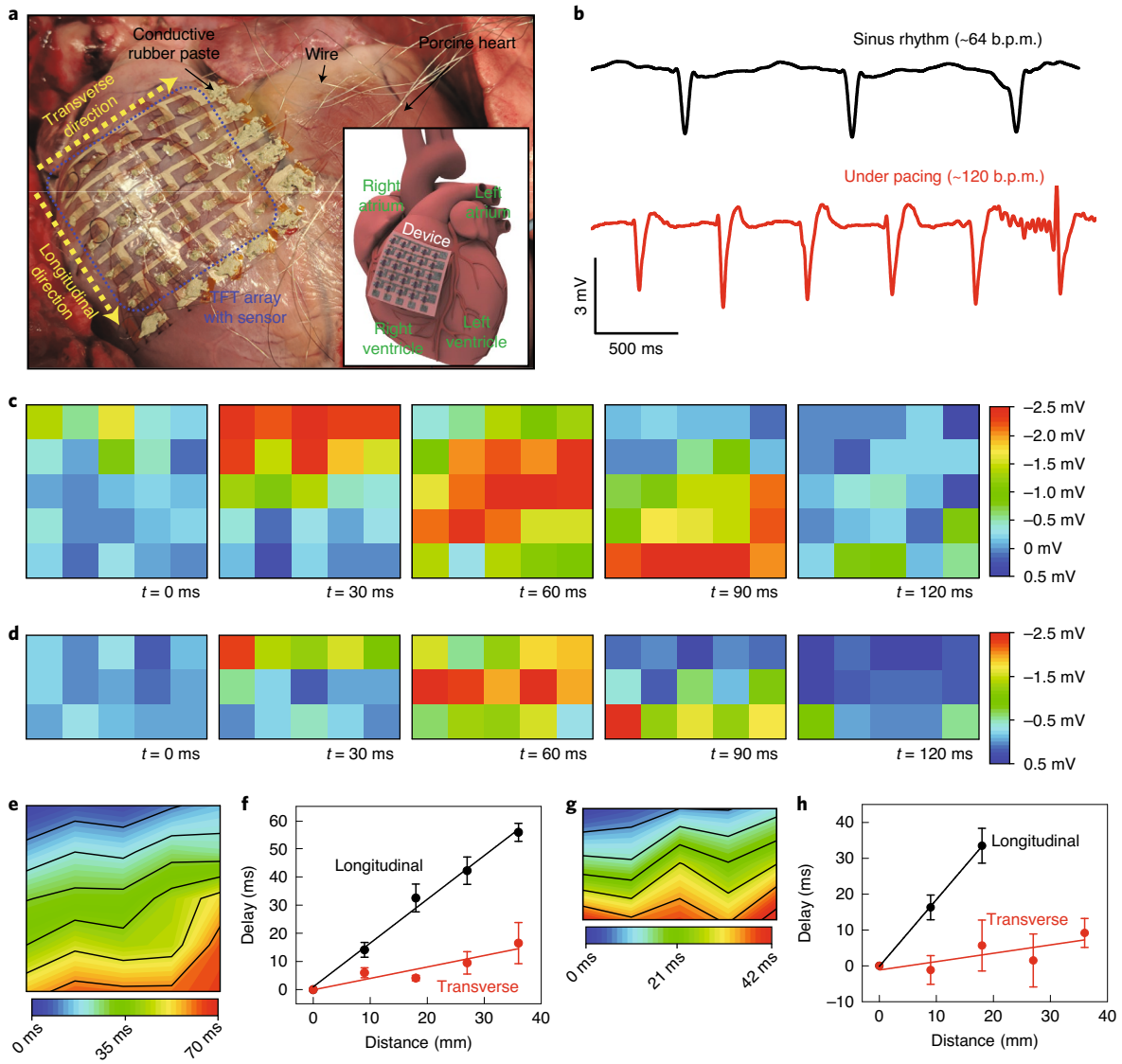

Fig. 4 | Electrophysiological mapping in vivo by the fully rubbery transistor active matrix. a, Optical image of a fully rubbery transistor active matrix on a porcine heart. Inset: a schematic illustration of the device position on the porcine heart. TFT, thin-film transistor. **b**, Representative single-voltage trace from the electrode array with and without pacing. **c**, Spatiotemporal biopotential mapping results from all sensing nodes at five sequential time points of the sinus rhythm. **d**, Spatiotemporal biopotential mapping results from all sensing nodes at five sequential time points during pacing by the first two rows of the devices. **e**, The map of the relative activation time of the sinus rhythm. The isochronal lines are drawn every 10 ms. **f**, The average activation delay depending on distance for longitudinal ($n = 5$) and transverse ($n = 5$) directions of the sinus rhythm. **g**, The map of the relative activation time during pacing. The isochronal lines are drawn every 7 ms. **h**, The average activation delay depending on distance for longitudinal ($n = 5$) and transverse ($n = 3$) directions during pacing. Data are presented as mean ± s.d. in **f** and **h**.

of tissue that do not properly conduct the cardiac potential (for example, scars), causing the heart to work harder to pump blood efficiently. After locating the dysfunctional tissue, treatments such as local electrical pacing can be administered to restore normal cardiac functions[49,50]. Therefore, we fabricated and characterized a 5 × 5 rubbery transistor array that offers spatial and temporal potential mapping and electrical pacing capabilities through a seamless interface between the device and organs, owing to the matching material properties. Although this work illustrates a 5 × 5 array, it is noted that the spatial resolution can be further enhanced with denser sensing nodes. The active-matrix-based ECG sensor and pacemaker array presented fairly uniform and reliable electrical characteristics of the arrayed devices, along with a high yield of 100%, as shown in Supplementary Figs. 18 and 19.

The optical image of the rubbery ECG sensor and pacemaker array based on the 5 × 5 active matrix implanted on an in vivo porcine heart is shown in Fig. 4a. A surgical adhesive (BioGlue, CryoLife) was applied between the device and porcine heart for enhanced adhesion. The inset depicts the spatial position of the rubbery sensor and pacemaker array on the right ventricle of the porcine heart. The data acquisition set-up for the in vivo experiment is shown in Supplementary Fig. 20. It is noted that the rubbery bioelectronics functions with wire connections; future development could lead to an untethered epicardial device. Representative voltage traces of the sinus rhythm (top, ~64 b.p.m.) and during pacing (bottom, ~120 b.p.m.), which were filtered using MATLAB to minimize external noise (Supplementary Fig. 21), are shown in Fig. 4b. The electrophysiological signal mapping results from all 25 nodes

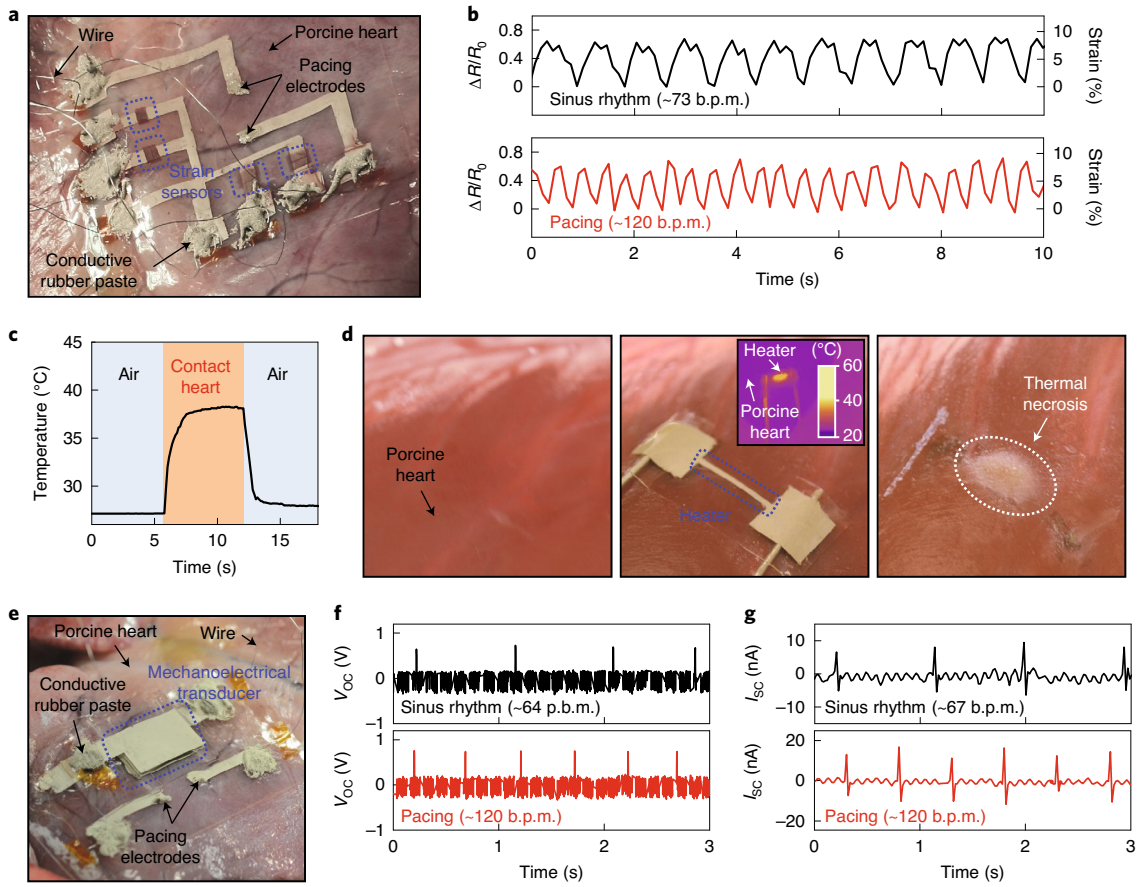

Fig. 5 | In vivo validation of the rubbery physical sensors and devices for ablation and harvesting. a, Optical image of the rubbery strain sensor on a porcine heart. **b**, Representative resistance change of the rubbery strain sensor on a porcine heart during the sinus rhythm (top) and during pacing (bottom). **c**, Temperature-change sensing of the rubbery temperature sensor before and after contact with the porcine heart. **d**, Thermal ablation using the rubbery heater before (left), during (middle) and after (right) applying a voltage of 3 V to the rubbery heater on the porcine heart. **e**, Optical image of a rubbery mechanoelectrical transducer on the porcine heart. **f**,**g**, Open-circuit voltage (**f**) and short-circuit current (**g**) of the rubbery mechanoelectrical transducer on the in vivo porcine heart.

are presented at five sequential time points of the sinus rhythm (Fig. 4c) and the ECG traces for each node are shown in Supplementary Fig. 22. The sequential maps clearly show the anisotropic signal propagation from top to bottom, coinciding well with the spatial position of the rubbery active matrix array on the porcine heart. Similar sequential maps at different time points during pacing are shown in Fig. 4d. For the pacing case, the first two rows of the array were used for bipolar epicardial pacing to illustrate the precise control of the pacing site using the array, without the need for a separate pacing system. On the basis of the ECG traces from all 25 sensing nodes, isochronal activation maps were constructed to investigate the conduction velocities of the signal of the porcine heart for both the sinus rhythm (Fig. 4e) and during pacing (Fig. 4g). The representative time delay in the longitudinal direction is shown in Supplementary Fig. 23. The relative activation delay depending on the distance for the sinus rhythm and during pacing is plotted in Fig. 4f,h, respectively. It is noted that each of the values for longitudinal and transverse directions are the average values of the rows and columns, respectively. The activation delay times for each column and row are plotted in Supplementary Fig. 24.

On the basis of the relative activation delay time, the obtained conduction velocity in the longitudinal direction (from top to bottom of the right ventricle) was 0.645 m s^{-1} and that in the transverse direction (from left to right of the right ventricle) was 2.47 m s^{-1}. The results clearly reveal the anisotropic conduction properties of the signal propagation and are in good agreement with previous studies of cardiac electrophysiology[11,12]. In addition, pacing caused the conduction velocity to change to 0.537 m s^{-1} and 4.28 m s^{-1} in the longitudinal and transverse directions, respectively (Fig. 4h and Supplementary Fig. 25). Again, this increase in the conduction velocity in both directions corresponds to the increased pacing frequency and faster heart rate compared with that of the sinus rhythm. The results present the great potential of the mapping and pacing functions for advanced implantable biomedical devices that are not only limited to cardiac applications, but can also be utilized for other organs that need to be spatially diagnosed and treated, such as the brain, stomach and bladder[51–53]. Furthermore, here we showed that the bioelectronic patch can serve as a temporary implant to provide critical information to surgeons during heart surgeries, which are a few hours in duration[54]. Over the course of a few hours, no damage to the heart was observed and the heartbeat was not noticeably influenced by the patch. It is noted that the biocompatibility of the epicardial bioelectronic patch can be further elucidated through studies of cell viability and inflammatory infiltrates[20].

In vivo physical property sensing and energy harvesting

Mechanical strain monitoring, which could be achieved using rubbery strain sensors, is a thoroughly investigated approach to diagnose cardiac disorders such as arrhythmic motion[39,55,56]. Figure 5a shows the rubbery strain sensor implanted on the porcine heart

in vivo. As shown in Fig. 5b, the change in strain as the heart beats is clearly detected by the rubbery strain sensor, which reveals a normalized resistance variation of around 60%: this corresponds to a strain change of approximately 8% at systole according to the strain sensor calibration curve described above (Fig. 2e). The recorded epicardial strains agree well with the reported literature[39]. The epicardial strain change during pacing only shows a change in frequency with an almost constant change in strain. An array of strain sensors could be easily constructed with a geometrical design modification; the array could provide substantial information about cardiac wall movement for a more comprehensive understanding of not only the local strain, but also the global strain over the heart[57].

Epicardial temperature is also one of the crucial parameters for cardiac health monitoring[40]. For instance, induced temperature modulation of the epicardial surface has been shown to modify the duration of the QT interval (observed in the ECG) and the conduction velocity, both of which can be used as indicators of ventricular arrhythmia[40,58]. Figure 5c shows the temperature detected by the rubbery temperature sensor before and after contacting the porcine heart surface, demonstrating its excellent temperature sensing properties. By using the same structure, the temperature sensor can be used as a thermal actuator that is a useful tool for tissue necrosis and possibly tumour destruction[59,60]. This design choice is favourable for device integration because only a single device design is needed to achieve both the functionalities of temperature sensing and thermal ablation. Figure 5d sequentially shows images of the epicardial surface before (left), during (middle) and after (right) thermal ablation by the rubbery thermal actuator: thermal necrosis can be clearly observed. The inset of Fig. 5d (middle) shows an infrared camera image of the thermal actuator generating around 60 °C, which is a sufficient temperature to cause necrosis (>50 °C)[43,44].

In addition to monitoring and treatment, the energy harvesting aspect based on a rubbery mechanoelectrical transducer was investigated as an alternative to the longstanding challenge of limited power supplies for implantable devices[45]. As a proof of concept, in vivo implantation of the rubbery mechanoelectrical transducer onto a porcine heart was performed to evaluate its electrical output properties (Fig. 5e). Figure 5f,g show the in vivo electrical output for the sinus rhythm and during pacing. The in vivo V_{oc} shows little change from 0.68 ± 0.03 V for the sinus rhythm to 0.74 ± 0.01 V during pacing, whereas the in vivo I_{sc} shows a relatively clear enhancement from 8.01 ± 1.17 nA for the sinus rhythm to 13.39 ± 2.59 nA during pacing. The more favourable frequency response of the I_{sc} is a typical phenomenon of the mechanoelectrical transducer based on the triboelectric effect[46]. The energy scavenged from the mechanoelectrical transducer can potentially be further optimized and managed to power the epicardial bioelectronic patch. These results corroborate the potential of the rubbery mechanoelectrical transducer as a power source to realize self-powered, implantable biomedical devices.

Conclusions

We have reported a soft and stretchable bioelectronic system consisting only of materials whose moduli are close to that of heart tissue. Unlike bioelectronics primarily based on rigid materials with mechanical structures that are stretchable on the macroscopic level, constructing bioelectronics out of materials with moduli matching those of the biological tissues suggests a promising route towards next-generational bioelectronics and biosensors that do not have a hard–soft interface for the heart and other organs. Our rubbery epicardial patch is capable of multiplexed ECG mapping, strain and temperature sensing, electrical pacing, thermal ablation and energy harvesting functions, and we have illustrated its capabilities on a living porcine heart. This combination of functions means that the device could potentially assist physicians in making decisions regarding the cardiac monitoring and treatment of patients, and could potentially help accelerate the discovery of new remedies. While our bioelectronic patch is primarily intended as a temporary epicardial implant, the inclusion of anti-inflammatory agents and materials, and a careful investigation of induced fibrosis, could potentially lead to the development of a chronic implant.

Methods

Materials. Regioregular P3HT ($M_w = 50{,}000$–$100{,}000$), 1-ethyl-3-methylimidazolium bis(trifluoromethylsulfonyl)imide ([EMIM][TFSI], >98%), poly(vinylidene fluoride-co-hexafluoropropylene) (PVDF-HFP) ($M_w = 400{,}000$), gold chloride trihydrate ($HAuCl_4 \cdot 3H_2O$, >99.9%), dichloromethane (anhydrous, >99.8%), acetone (ACS reagent, >99.5%) and ammonium hydroxide solution (ACS reagent, 28.0–30.0%) were all from Sigma-Aldrich and used without further purification. AgNW (~99.5%) solution (average diameter, 120 nm; length, 20 μm) was from ACS Material. PDMS rubber (Sylgard 184 silicone elastomer kit) was from Dow Corning. The conductive rubber pastes (FL45) were from Zoflex. The surgical adhesive (BioGlue) was from CryoLife.

Preparation of P3HT-NFs/PDMS composite semiconductor solution. To form P3HT-NFs, a 2-mg-ml^{-1} P3HT solution based on dichloromethane was heated to 60 °C to form a homogeneously dissolved P3HT solution, followed by storage at −20 °C for 30 min to form self-assembled P3HT-NFs through π–π stacking due to the reduced solubility[61]. The PDMS (10:1 weight ratio of base and curing agent) solution in dichloromethane was added to P3HT-NF solution for formation of the P3HT-NFs/PDMS in the weight ratio of 2:8. The solution was stored at −20 °C.

Preparation of rubbery AgNWs/PDMS composite conductor. The preparation of the rubbery AgNWs/PDMS composite conductor involved cleaning a glass substrate with acetone, isopropyl alcohol and deionized water, followed by dehydration at 110 °C for 2 min on a hot plate. Thereafter, the AgNW pattern was formed by drop casting using the AgNW solution (15 mg ml^{-1}) on clean glass through Kapton-tape-based shadow masks that were prepared by a programmable cutting machine (Silhouette Cameo). The pattern was dried at 60 °C for 10 min, followed by baking at 200 °C for 30 min to obtain enhanced electrical conductivity by thermal welding between the wires. The PDMS solution (15:1 weight ratio of base and curing agent) was coated onto the patterned AgNWs by spin casting at 400 r.p.m. for 60 s, then the sample was solidified at 60 °C for 4 h. It is noted that the ratio of 15:1 is chosen to achieve PDMS with appropriate softness and the formation of rubbery electrodes. The porous structured AgNW network allows the PDMS solution to permeate into the network, which results in AgNWs partially embedded in the solidified PDMS. The solidified PDMS with AgNW pattern was then peeled off from the glass slide to complete the preparation of the rubbery AgNWs/PDMS composite conductor.

Preparation of ion-gel dielectric. The ion gel was prepared by mixing PVDF-HFP, [EMIM][TFSI] and acetone as the polymeric matrix, ionic liquid and solvent, respectively, in a weight ratio of 1:4:7 at 70 °C for 1 h. The ionic liquid was dehydrated in a vacuum oven at 70 °C overnight. The prepared solution was cast onto a clean glass substrate and solidified in vacuum oven at 70 °C for 12 h, followed by cutting the ion gel into the appropriate shapes. The typical thickness of the ion gel was approximately 150 μm.

Mechanical property investigation of ion-gel dielectric. The stress–strain curves of the rubbery materials were obtained with a tensile strength tester (Mark 10 with Series 5 digital force gauges) under continuous application of tensile strain with a speed of 20 mm min^{-1}.

Fabrication process of the soft and stretchy epicardial bioelectronic patch. The fabrication of the soft and stretchy epicardial bioelectronic patch began by preparing a double-side embedded AgNWs/PDMS composite electrode. First, the AgNWs/PDMS composite electrode for the top electrode was prepared by the aforementioned process. Then, AgNWs were patterned onto another glass substrate for the bottom electrodes. After spin casting of PDMS on the AgNW pattern, the AgNWs/PDMS for the top electrodes was carefully aligned and laminated on top of the spin-cast PDMS. The sample was solidified at 60 °C for 4 h, followed by peeling off from the glass slide. The prepared double-sided embedding of AgNWs in PDMS had a thickness of ~350 μm. To form an ohmic contact between the P3HT-NFs/PDMS semiconducting layer and AgNWs/PDMS composite conductor, AuNPs were coated on the exposed AgNWs by galvanic exchange, which involved dropping $HAuCl_4 \cdot 3H_2O$ solution (0.5 mM) onto the AgNWs/PDMS, then rinsing with deionized water after 2 min to allow for Ag–Au galvanic replacement. 28% NH_4OH solution was used to dissolve the by-products of the AgCl layer on the AgNWs, followed by sequentially rinsing, drying and dehydrating, to complete the preparation of AuNPs–AgNWs/PDMS. The P3HT-NFs/PDMS composite solution was treated using ultrasonication for 20 s before forming a film on the channel region for the transistor array and strain sensors. Spin casting through the Kapton-film-based shadow mask allowed for well patterned P3HT-NFs/PDMS, which was annealed at 90 °C for 30 min. Thereafter,

via holes were created to interconnect the top and bottom electrodes of each sensing node. Conductive rubber paste was used to fill the via holes, followed by solidification at room temperature for 12 h. The fully solidified conductive rubber paste has very strong adhesion to the PDMS substrate without any delamination under a mechanical strain of 50%. The appropriately shaped ion gel pieces serving as the gate dielectrics were aligned and laminated on the devices. To form the encapsulation layer, a thin PDMS layer (15:1 weight ratio of base and curing agent) was coated at 2,000 r.p.m. for 30 s on top of the devices, with a Kapton-film-based shadow mask covering the interfacing electrodes and electrodes for the rubbery mechanoelectrical transducer. This was followed by solidification at 60 °C for 4 h. Pieces of the AgNWs/PDMS electrodes for the mechanoelectrical transducer were placed on the device with thin PDMS spacers (<1 mm).

Device characterization. The electrical characteristics of the rubbery transistor, strain sensor and temperature sensor were determined with a semiconductor analyser (Keithley 4200-SCS) with a custom-made stretcher to characterize the performance under different mechanical strains. The dynamic strain change of the rubbery strain sensor was obtained using an IPC flexural endurance tester (CK-700FET, CKSI). The Joule heating property of the rubbery thermal actuator was investigated by measuring the temperature change depending on the applied voltage using a Fluke 566 infrared thermometer with a type K thermocouple probe and a d.c. power supply (1627A, B&K Precision). The mechanoelectrical transducer was electrically characterized with a Keithley 6514 electrometer and externally connected resistors under mechanical stretching by the IPC flexural endurance tester. For the sensing node verification, an input signal was applied by a function generator (DG4062, RIGOL) that was monitored using an oscilloscope (DSO-X 2004A, Agilent). The output voltage was obtained by the Keithley 4200-SCS. All ECG signals were obtained with an RHD2000 evaluation board and RHD2132 amplifier board (Intan). The temperature mapping of the rubbery thermal actuator during thermal ablation at an applied voltage of 3 V was captured by an infrared camera (FLIR ONE Pro, FLIR Systems).

In vivo animal experiment. All devices were wired with perfluoroalkoxy alkane-coated stainless steel wires (bare diameter 76.2 µm and coated diameter 139.7 µm, A-M Systems) with conductive rubber paste for the interface to the equipment. After the pig was placed under anaesthesia, the chest was opened to expose the heart. The majority of the biofluids on the porcine heart were removed using gauze and then BioGlue was applied for enhanced adhesion between the devices and the surface of the heart. Once the devices were placed on the heart, data were collected. The animal in this study was handled and maintained in accordance with the requirements of the Laboratory Animal Welfare Act (P.L. 89-544) and its 1970 (P.L. 91-579), 1976 (P.L. 94-279) and 1985 (P.L. 99-198) amendments and within the specifications indicated below. Compliance was accomplished by conforming to the standards in the Guide for the Care and the Use of Laboratory Animals, ILAR, National Academy Press, revised 2011. All procedures were approved by the Texas Heart Institute Institutional Animal Care and Use Committee.

Data processing. To process the ECGs from each sensing node of the rubbery transistor array, the raw data were first imported into MATLAB. Custom infinite impulse response filters were designed and their frequency response was observed. A 60-Hz notch filter (third order) was applied to remove power-line noise from the raw data. Following this, a third-order bandpass filter with cutoff frequencies of 1 and 40 Hz was applied to recover the physiologically relevant cardiac potentials.

Reporting Summary. Further information on research design is available in the Nature Research Reporting Summary linked to this article.

Data availability

The data that support the plots within this paper and other findings of this study are available from the corresponding author upon reasonable request.

Code availability

Custom code used to process the data is available from the corresponding author upon reasonable request.

Received: 5 February 2020; Accepted: 24 September 2020;
Published online: 03 November 2020

References

1. Heron, M. & Anderson, R. N. *Changes in the Leading Cause of Death: Recent Patterns in Heart Disease and Cancer Mortality* Data Brief 254 (NCHS, 2016).
2. Mozaffarian, D. et al. Executive summary: Heart disease and stroke statistics—2016 update. *Circulation* **133**, 447–454 (2016).
3. Mair, H., Jansens, J.-L., Lattouf, O. M., Reichart, B. & Dabritz, S. Epicardial lead implantation techniques for biventricular pacing via left lateral mini-thoracotomy, video-assisted thoracoscopy, and robotic approach. *Heart Surg. Forum* **6**, 412–417 (2003).
4. Costa, R., Scanavacca, M., da Silva, K. R., Martinelli Filho, M. & Carrillo, R. Novel approach to epicardial pacemaker implantation in patients with limited venous access. *Heart Rhythm* **10**, 1646–1652 (2013).
5. Boyle, N. G. & Shivkumar, K. Epicardial interventions in electrophysiology. *Circulation* **126**, 1752–1769 (2012).
6. Cantwell, C. D. et al. Techniques for automated local activation time annotation and conduction velocity estimation in cardiac mapping. *Comput. Biol. Med.* **65**, 229–242 (2015).
7. Dubois, R. et al. Non-invasive cardiac mapping in clinical practice: application to the ablation of cardiac arrhythmias. *J. Electrocardiol.* **48**, 966–974 (2015).
8. Ershad, F., Sim, K., Thukral, A., Zhang, Y. S. & Yu, C. Invited article: emerging soft bioelectronics for cardiac health diagnosis and treatment. *APL Mater.* **7**, 031301 (2018).
9. Erem, B., Brooks, D. H., van Dam, P. M., Stinstra, J. G. & MacLeod, R. S. Spatiotemporal estimation of activation times of fractionated ECGs on complex heart surfaces. In *2011 Annual International Conference of the IEEE Engineering in Medicine and Biology Society* 5884-5887 (IEEE, 2011).
10. Gu, S. et al. Mapping conduction velocity of early embryonic hearts with a robust fitting algorithm. *Biomed. Opt. Express* **6**, 2138–2157 (2015).
11. Fang, H. et al. Capacitively coupled arrays of multiplexed flexible silicon transistors for long-term cardiac electrophysiology. *Nat. Biomed. Eng.* **1**, 0038 (2017).
12. Viventi, J. et al. A conformal, bio-interfaced class of silicon electronics for mapping cardiac electrophysiology. *Sci. Transl. Med.* **2**, 24ra22 (2010).
13. Kim, D. H. et al. Electronic sensor and actuator webs for large-area complex geometry cardiac mapping and therapy. *Proc. Natl Acad. Sci. USA* **109**, 19910–19915 (2012).
14. Xu, L. et al. 3D multifunctional integumentary membranes for spatiotemporal cardiac measurements and stimulation across the entire epicardium. *Nat. Commun.* **5**, 3329 (2014).
15. Xu, L. et al. Materials and fractal designs for 3D multifunctional integumentary membranes with capabilities in cardiac electrotherapy. *Adv. Mater.* **27**, 1731–1737 (2015).
16. Lee, W. et al. Nonthrombogenic, stretchable, active multielectrode array for electroanatomical mapping. *Sci. Adv.* **4**, eaau2426 (2018).
17. Blakney, A. K., Swartzlander, M. D. & Bryant, S. J. The effects of substrate stiffness on the in vitro activation of macrophages and in vivo host response to poly(ethylene glycol)-based hydrogels. *J. Biomed. Mater. Res. A* **100**, 1375–1386 (2012).
18. Engler, A. J. et al. Embryonic cardiomyocytes beat best on a matrix with heart-like elasticity: scar-like rigidity inhibits beating. *J. Cell Sci.* **121**, 3794–3802 (2008).
19. Kim, D. H. et al. Epidermal electronics. *Science* **333**, 838–843 (2011).
20. Park, J. et al. Electromechanical cardioplasty using a wrapped elasto-conductive epicardial mesh. *Sci. Transl. Med.* **8**, 344ra386 (2016).
21. Davenport Huyer, L. et al. Highly elastic and moldable polyester biomaterial for cardiac tissue engineering applications. *ACS Biomater. Sci. Eng.* **2**, 780–788 (2016).
22. Kapnisi, M. et al. Auxetic cardiac patches with tunable mechanical and conductive properties toward treating myocardial infarction. *Adv. Funct. Mater.* **28**, 1800618 (2018).
23. Reis, L. A., Chiu, L. L. Y., Feric, N., Fu, L. & Radisic, M. Biomaterials in myocardial tissue engineering. *J. Tissue Eng. Regen. Med.* **10**, 11–28 (2016).
24. Sim, K. et al. Fully rubbery integrated electronics from high effective mobility intrinsically stretchable semiconductors. *Sci. Adv.* **5**, eaav5749 (2019).
25. Kim, H.-J., Thukral, A., Sharma, S. & Yu, C. Biaxially stretchable fully elastic transistors based on rubbery semiconductor nanocomposites. *Adv. Mater. Technol.* **3**, 1800043 (2018).
26. Kim, H.-J., Sim, K., Thukral, A. & Yu, C. Rubbery electronics and sensors from intrinsically stretchable elastomeric composites of semiconductors and conductors. *Sci. Adv.* **3**, e1701114 (2017).
27. Lee, H. et al. Highly stretchable and transparent supercapacitor by Ag–Au core–shell nanowire network with high electrochemical stability. *ACS Appl. Mater. Interfaces* **8**, 15449–15458 (2016).
28. Momtahan, N. et al. Automation of pressure control improves whole porcine heart decellularization. *Tissue Eng. C* **21**, 1148–1161 (2015).
29. Ji, Y. et al. High-performance p-type copper(I) thiocyanate thin film transistors processed from solution at low temperature. *Adv. Mater. Interfaces* **6**, 1900883 (2019).
30. Lenz, J., del Giudice, F., Geisenhof, F. R., Winterer, F. & Weitz, R. T. Vertical, electrolyte-gated organic transistors show continuous operation in the mA cm^{-2} regime and artificial synaptic behaviour. *Nat. Nanotechnol.* **14**, 579–585 (2019).
31. Kim, S. H., Hong, K., Lee, K. H. & Frisbie, C. D. Performance and stability of aerosol-jet-printed electrolyte-gated transistors based on poly(3-hexylthiophene). *ACS Appl. Mater. Interfaces* **5**, 6580–6585 (2013).
32. Xu, J. et al. Highly stretchable polymer semiconductor films through the nanoconfinement effect. *Science* **355**, 59 (2017).

33. Xu, J. et al. Multi-scale ordering in highly stretchable polymer semiconducting films. *Nat. Mater.* **18**, 594–601 (2019).
34. Oh, J. Y. et al. Stretchable self-healable semiconducting polymer film for active-matrix strain-sensing array. *Sci. Adv.* **5**, eaav3097 (2019).
35. Wang, S. et al. Skin electronics from scalable fabrication of an intrinsically stretchable transistor array. *Nature* **555**, 83 (2018).
36. Nguyen, J. S., Lakkis, N. M., Bobek, J., Goswami, R. & Dokainish, H. Systolic and diastolic myocardial mechanics in patients with cardiac disease and preserved ejection fraction: impact of left ventricular filling pressure. *J. Am. Soc. Echocardiogr.* **23**, 1273–1280 (2010).
37. Howard-Quijano, K. et al. Left ventricular endocardial and epicardial strain changes with apical myocardial ischemia in an open-chest porcine model. *Physiol. Rep.* **4**, e13042 (2016).
38. D'Hooge, J. et al. Regional strain and strain rate measurements by cardiac ultrasound: principles, implementation and limitations. *Eur. J. Echocardiogr.* **1**, 154–170 (2000).
39. Ferraiuoli, P. et al. Full-field analysis of epicardial strain in an in vitro porcine heart platform. *J. Mech. Behav. Biomed. Mater.* **91**, 294–300 (2019).
40. Fenton, F. H., Gizzi, A., Cherubini, C., Pomella, N. & Filippi, S. Role of temperature on nonlinear cardiac dynamics. *Phys. Rev. E* **87**, 042717 (2013).
41. Lim, H. S. et al. Noninvasive mapping to guide atrial fibrillation ablation. *Card. Electrophysiol. Clin.* **7**, 89–98 (2015).
42. Narayan, S. M. et al. Treatment of atrial fibrillation by the ablation of localized sources: CONFIRM (conventional ablation for atrial fibrillation with or without focal impulse and rotor modulation) trial. *J. Am. Coll. Cardiol.* **60**, 628–636 (2012).
43. Diederich, C. J. Thermal ablation and high-temperature thermal therapy: overview of technology and clinical implementation. *Int. J. Hyperth.* **21**, 745–753 (2005).
44. Webb, H., Lubner, M. G. & Hinshaw, J. L. Thermal ablation. *Semin. Roentgenol.* **46**, 133–141 (2011).
45. Toprak, A. & Tigli, O. Piezoelectric energy harvesting: state-of-the-art and challenges. *Appl. Phys. Rev.* **1**, 031104 (2014).
46. Wu, C., Wang, A. C., Ding, W., Guo, H. & Wang, Z. L. Triboelectric nanogenerator: a foundation of the energy for the new era. *Adv. Energy Mater.* **9**, 1802906 (2019).
47. Zhang, C. & Wang, Z. L. in *Micro Electro Mechanical Systems* (ed. Huang, Q.-A.) 1335–1376 (Springer, 2018).
48. Sánchez-Quintana, D., Doblado-Calatrava, M., Cabrera, J. A., Macías, Y. & Saremi, F. Anatomical basis for the cardiac interventional electrophysiologist. *Biomed Res. Int.* **2015**, 547364 (2015).
49. Tang, A. S. L. et al. Cardiac-resynchronization therapy for mild-to-moderate heart failure. *N. Engl. J. Med.* **363**, 2385–2395 (2010).
50. Jayaprakash, S. Clinical presentations, diagnosis, and management of arrhythmias associated with cardiac tumors. *J. Arrhythm.* **34**, 384–393 (2018).
51. Cheng, L. K. et al. Detailed measurements of gastric electrical activity and their implications on inverse solutions. In *2009 Annual International Conference of the IEEE Engineering in Medicine and Biology Society* 1302–1305 (IEEE, 2009).
52. Ballaro, A., Mundy, A. R., Fry, C. H. & Craggs, M. D. Bladder electrical activity: the elusive electromyogram. *BJU Int.* **92**, 78–84 (2003).
53. Thukral, A., Ershad, F., Enan, N., Rao, Z. & Yu, C. Soft ultrathin silicon electronics for soft neural interfaces: a review of recent advances of soft neural interfaces based on ultrathin silicon. *IEEE Nanotechnol. Mag.* **12**, 21–34 (2018).
54. Baba, T. et al. Early neuropsychological dysfunction in elderly high-risk patients after on-pump and off-pump coronary bypass surgery. *J. Anesth.* **21**, 452–458 (2007).
55. Zhang, H., Iijima, K., Huang, J., Walcott, G. P. & Rogers, J. M. Optical mapping of membrane potential and epicardial deformation in beating hearts. *Biophys. J.* **111**, 438–451 (2016).
56. Dandel, M., Lehmkuhl, H., Knosalla, C., Suramelashvili, N. & Hetzer, R. Strain and strain rate imaging by echocardiography—basic concepts and clinical applicability. *Curr. Cardiol. Rev.* **5**, 133–148 (2009).
57. Aletras, A. H., Balaban, R. S. & Wen, H. High-resolution strain analysis of the human heart with fast-DENSE. *J. Magn. Reson.* **140**, 41–57 (1999).
58. Guill, A. et al. QT interval heterogeneities induced through local epicardial warming/cooling. An experimental study. *Rev. Esp. Cardiol. (Engl. Ed.)* **67**, 993–998 (2014).
59. Kassiri, Z. et al. Combination of tumor necrosis factor-α ablation and matrix metalloproteinase inhibition prevents heart failure after pressure overload in tissue inhibitor of metalloproteinase-3 knock-out mice. *Circ. Res.* **97**, 380–390 (2005).
60. Skonieczki, B. D., Wells, C., Wasser, E. J. & Dupuy, D. E. Radiofrequency and microwave tumor ablation in patients with implanted cardiac devices: is it safe? *Eur. J. Radiol.* **79**, 343–346 (2011).
61. Oh, J. Y. et al. Self-seeded growth of poly(3-hexylthiophene) (P3HT) nanofibrils by a cycle of cooling and heating in solutions. *Macromolecules* **45**, 7504–7513 (2012).

Acknowledgements

C.Y. would like to acknowledge the support by the National Science Foundation CAREER grant (CMMI-1554499), the Office of Naval Research grant (N00014-18-1-2338) under the Young Investigator Program, the National Institutes of Health grant (R21EB026175) and 3M non-tenured faculty award. F.E. acknowledges the National Science Foundation Graduate Research Fellowship Program.

Author contributions

C.Y., K.S., F.E., Y.X. and P.Y. conceived and designed the experiments. K.S., Y.Z., H.S., Z.R., Y.L. and A.T. fabricated devices. K.S., F.E., Y.Z., P.Y., H.S. and Z.R. performed the characterization experiments. K.S., F.E., Y.Z., Y.X., P.Y., H.S., Z.R. and A.E. performed the in vivo animal experiments. K.S., F.E., Y.X., H.S. and C.Y. analysed the experimental data. K.S., F.E. and C.Y. wrote the paper. All the authors reviewed and revised the manuscript.

Competing interests

The authors declare no competing interests.

Additional information

Supplementary information is available for this paper at https://doi.org/10.1038/s41928-020-00493-6.

Correspondence and requests for materials should be addressed to C.Y.

Reprints and permissions information is available at www.nature.com/reprints.

Publisher's note Springer Nature remains neutral with regard to jurisdictional claims in published maps and institutional affiliations.

nature research

Corresponding author(s): Cunjiang Yu

Last updated by author(s): Sep 1, 2020

Reporting Summary

Nature Research wishes to improve the reproducibility of the work that we publish. This form provides structure for consistency and transparency in reporting. For further information on Nature Research policies, see Authors & Referees and the Editorial Policy Checklist.

Statistics

For all statistical analyses, confirm that the following items are present in the figure legend, table legend, main text, or Methods section.

n/a	Confirmed	
☐	☒	The exact sample size (*n*) for each experimental group/condition, given as a discrete number and unit of measurement
☒	☐	A statement on whether measurements were taken from distinct samples or whether the same sample was measured repeatedly
☒	☐	The statistical test(s) used AND whether they are one- or two-sided *Only common tests should be described solely by name; describe more complex techniques in the Methods section.*
☒	☐	A description of all covariates tested
☒	☐	A description of any assumptions or corrections, such as tests of normality and adjustment for multiple comparisons
☐	☒	A full description of the statistical parameters including central tendency (e.g. means) or other basic estimates (e.g. regression coefficient) AND variation (e.g. standard deviation) or associated estimates of uncertainty (e.g. confidence intervals)
☒	☐	For null hypothesis testing, the test statistic (e.g. *F*, *t*, *r*) with confidence intervals, effect sizes, degrees of freedom and *P* value noted *Give P values as exact values whenever suitable.*
☒	☐	For Bayesian analysis, information on the choice of priors and Markov chain Monte Carlo settings
☒	☐	For hierarchical and complex designs, identification of the appropriate level for tests and full reporting of outcomes
☒	☐	Estimates of effect sizes (e.g. Cohen's *d*, Pearson's *r*), indicating how they were calculated

Our web collection on statistics for biologists contains articles on many of the points above.

Software and code

Policy information about availability of computer code

Data collection	Intan Technologies RHD2000 Interface v1.5.2
Data analysis	MATLAB 2018a

For manuscripts utilizing custom algorithms or software that are central to the research but not yet described in published literature, software must be made available to editors/reviewers. We strongly encourage code deposition in a community repository (e.g. GitHub). See the Nature Research guidelines for submitting code & software for further information.

Data

Policy information about availability of data

All manuscripts must include a data availability statement. This statement should provide the following information, where applicable:

- Accession codes, unique identifiers, or web links for publicly available datasets
- A list of figures that have associated raw data
- A description of any restrictions on data availability

The authors declare that all data supporting the findings of these studies are available within the paper and its Supplementary Information.

Field-specific reporting

Please select the one below that is the best fit for your research. If you are not sure, read the appropriate sections before making your selection.

☒ Life sciences ☐ Behavioural & social sciences ☐ Ecological, evolutionary & environmental sciences

For a reference copy of the document with all sections, see nature.com/documents/nr-reporting-summary-flat.pdf

Life sciences study design

All studies must disclose on these points even when the disclosure is negative.

Sample size	The sample size was chosen to be 1 to validate the functionality of the epicardial bioelectronic patch. The sample size (1) for the pig was determined to be sufficient as the results were reproducible and the animal experiments were intended to demonstrate device capabilities.
Data exclusions	No data were excluded from the analyses.
Replication	All electrophysiological recordings were successfully repeated 5 times for the non-pacing and pacing conditions.
Randomization	Randomization was not relevant to this study as the primary aim was to demonstrate the functionality of the epicardial bioelectronic patch.
Blinding	Not relevant, because a blinding process would not influence the sampling result.

Reporting for specific materials, systems and methods

We require information from authors about some types of materials, experimental systems and methods used in many studies. Here, indicate whether each material, system or method listed is relevant to your study. If you are not sure if a list item applies to your research, read the appropriate section before selecting a response.

Materials & experimental systems

n/a	Involved in the study
☒	☐ Antibodies
☒	☐ Eukaryotic cell lines
☒	☐ Palaeontology
☐	☒ Animals and other organisms
☒	☐ Human research participants
☒	☐ Clinical data

Methods

n/a	Involved in the study
☒	☐ ChIP-seq
☒	☐ Flow cytometry
☒	☐ MRI-based neuroimaging

Animals and other organisms

Policy information about studies involving animals; ARRIVE guidelines recommended for reporting animal research

Laboratory animals	1 domestic yorkshire pig, age: 6 months, sex: female
Wild animals	This study did not involve wild animals.
Field-collected samples	This study did not involve field-collected samples.
Ethics oversight	Compliance was accomplished by conforming to the standards in the Guide for the Care and the Use of Laboratory Animals, ILAR, National Academy Press, revised 2011. All procedures were approved by the Texas Heart Institute Institutional Animal Care and Use Committee.

Note that full information on the approval of the study protocol must also be provided in the manuscript.